

## Superhard Nitride-Based Nanocomposites: Role of Interfaces and Effect of Impurities

Shiqiang Hao,<sup>1</sup> Bernard Delley,<sup>2</sup> Stan Veprek,<sup>3</sup> and Catherine Stampfl<sup>1</sup>

<sup>1</sup>*School of Physics, The University of Sydney, Sydney NSW 2006, Australia*

<sup>2</sup>*Paul Scherrer Institut, WHGA/123, CH-5232 Villigen PSI, Switzerland*

<sup>3</sup>*Department of Chemistry, Technical University Munich, Lichtenbergstrasse 4, D-85747 Garching, Germany*

(Received 20 April 2006; published 24 August 2006)

Recently, a hardness similar to that of diamond has been reported for a quasiternary, nitride-based nanocomposite. The related, quasibinary nanocomposite “*nc*-TiN/*a*-Si<sub>3</sub>N<sub>4</sub>,” which may be regarded as the prototype of the family of superhard *nc*-metal-N/*a*-Si<sub>3</sub>N<sub>4</sub> systems, also exhibits a significant hardness enhancement. Extensive density-functional theory calculations indicate that the superhardness is related to the preferential formation of TiN(111) polar interfaces with a thin  $\beta$ -Si<sub>3</sub>N<sub>4</sub>-derived layer. The strength of TiN in the  $\langle 111 \rangle$  direction is similar to that of the weakest bonding direction in diamond. Oxygen impurities cause a significant reduction of the interface strength.

DOI: 10.1103/PhysRevLett.97.086102

PACS numbers: 68.35.-p, 62.20.Qp, 71.15.Nc

There has been considerable effort in recent years in identifying and developing new and improved super- and ultrahard materials [1–9]. Such structures clearly have huge potential technological and industrial applications [10] but are also of fundamental interest with regard to understanding the mechanisms responsible for the enhanced hardness. In particular, the most challenging quest, to find a material harder than diamond, is proving elusive. One strategy, however, that has led to reported hardnesses equal to, and exceeding, that of diamond ( $\geq 100$  GPa) [5] is based upon a generic design concept involving self-organized spinodal phase segregation, leading to a nanocomposite “*nc*-TiN/*a*-Si<sub>3</sub>N<sub>4</sub>/*a*- and *nc*-TiSi<sub>2</sub>,” with strong, sharp interfaces between nanocrystalline regions and thin amorphous layers. The related, more simple quasibinary nanocomposite *nc*-TiN/*a*-Si<sub>3</sub>N<sub>4</sub>, which exhibits a reported superhardness of 50–60 GPa [5,6,11–13], is the most quantitatively studied and may be regarded as the “prototype” for the nitride-based family of nanocomposites, which include *nc*-MN/*a*-Si<sub>3</sub>N<sub>4</sub> ( $M = \text{W, V, Al}_{1-x}\text{Ti}_x$ ) and *nc*-TiN/*a*-BN. Not all investigations, however, have found such a high hardness: For example, Ref. [14] obtained  $< 32$  GPa for the model *nc*-TiN/*a*-Si<sub>3</sub>N<sub>4</sub> nanocomposite, and, for TiN-Si<sub>3</sub>N<sub>4</sub> heterostructures reported in Refs. [15,16], the maximum hardness reached only about 33 GPa. Clearly, it is of significant importance to understand the origin and extent of the superstrengthening effect in ceramic nanocomposites, and critical experimental and theoretical evidence is needed to verify and understand reported results, which should include detailed structural and mechanical characterization.

In the present Letter, we perform extensive density-functional theory (DFT) calculations to investigate the atomic structure of the interface between the TiN nanocrystalline and silicon-nitride-like regions. For typical experimental conditions, our investigations show the importance of the preferential formation of TiN(111) polar

interfaces with that of a thin  $\beta$ -like Si<sub>2</sub>N<sub>3</sub> layer resembling a partial layer of  $\beta$ -Si<sub>3</sub>N<sub>4</sub>(10 $\bar{1}$ 0), in which the Si atoms are purely N-coordinated and tetrahedrally bonded. The strength in the  $\langle 111 \rangle$  crystallographic direction of titanium nitride is significantly higher than in other directions and similar to that of the weakest bonding direction in diamond. Oxygen impurities are predicted to diffuse to the interface region and cause a significant reduction of the strength. This effect, together with possible nonrealization of these polar interfaces due, e.g., to too low growth temperatures or too low nitrogen pressures, is proposed to explain the varying hardness values reported [11].

The DFT calculations are performed using the DMol<sup>3</sup> code [17] with the generalized gradient approximation for the exchange-correlation functional [18]. We use the double-numeric quality basis set with polarization functions and pseudopotentials which include scalar relativistic corrections. Convergence tests show that an atomic cutoff radius of 9 Bohr is sufficient [19]. Calculations of the bulk properties of TiN and  $\alpha$ -,  $\beta$ -, and  $\gamma$ -Si<sub>3</sub>N<sub>4</sub> are in excellent agreement with experiment [19].

High-resolution transmission electron microscopy studies [20] of interfaces in *nc*-TiN/*a*-Si<sub>3</sub>N<sub>4</sub> nanocomposites show that the main crystallographic planar orientation relationship is (10 $\bar{1}$ 0)Si<sub>3</sub>N<sub>4</sub> || (1 $\bar{1}$ 1)TiN. The {111} lattice planes of TiN are polar, terminated by either nitrogen or titanium atoms; similarly, the {10 $\bar{1}$ 0} lattice planes of  $\alpha$ - and  $\beta$ -Si<sub>3</sub>N<sub>4</sub> are polar containing either nitrogen or silicon atoms. Therefore, in the interface, it is conceivable that nitrogen atoms are shared between silicon nitride and titanium nitride.

In order to identify low energy interface structures, we calculate the interfacial formation energy  $E^f$ :

$$E^f = \left( E_{\text{tot}}^{\text{int}} - E_{\text{slab}}^{\text{TiN}} - \sum_i n_i \mu_i \right) / S, \quad (1)$$

where  $E_{\text{tot}}^{\text{int}}$  and  $E_{\text{slab}}^{\text{TiN}}$  are the total energies of the interfacial

system under consideration and a 20-layer TiN(111) slab with interface area  $S$ , respectively;  $n_i$  and  $\mu_i$  are the number and chemical potential of atoms of species  $i$  (i.e., N, Si, Ti), respectively, that are added to the TiN slab in order to create the interface of interest. The interface region is sandwiched between two 10-layer TiN(111) slabs and surrounded by a vacuum region of 20 Å.

To make contact with experiment, we consider nitrogen-rich and nitrogen-poor (or Ti-rich) conditions. For the former, we use  $\mu_N = \frac{1}{2}E_{N_2}$  (half the total energy of the  $N_2$  molecule), and for the latter we use  $\mu_{Ti} = E_{Ti}^{bulk}$ , which is the total energy of a bulk hcp Ti atom. We assume that in equilibrium  $\mu_{TiN} = \mu_{Ti} + \mu_N$ , where  $\mu_{TiN}$  is the chemical potential of bulk rocksalt TiN. For N-rich conditions, we then have  $\mu_{Ti} = E_{TiN} - \frac{1}{2}E_{N_2}$ , and, similarly, for N-poor conditions we have  $\mu_N = E_{TiN} - E_{Ti}^{bulk}$  [21]. The N-chemical potential can be correlated to its dependence on the  $N_2$  gas pressure and temperature as

$$\mu_N(T, p_{N_2}) = \frac{1}{2} \left[ E_{N_2}^{total} + \tilde{\mu}_N(T, p^0) + k_B T \ln \left( \frac{p_{N_2}}{p^0} \right) \right], \quad (2)$$

as obtained by manipulation of the ideal gas equations [22]. Here  $p_{N_2}$  is the nitrogen pressure,  $p^0$  corresponds to atmospheric pressure, and  $k_B$  is the Boltzmann constant. The temperature dependence of  $\tilde{\mu}_N(T, p^0)$  is taken from thermodynamic data [23].

We first consider three simple ( $1 \times 1$ ) interface structures: (i) inserting a Si layer between the two 10-layer TiN(111) slabs (resulting in *N-Si-Ti* bonding), (ii) a SiN layer (resulting in *N-Si-N-Ti* bonding), and (iii) a TiSi layer (resulting in *N-Ti-Si-Ti* bonding); see Figs. 1(d), 1(a), and 1(e), respectively. In this notation, the N and Ti layers at the interface side of the lower and upper slabs, respectively, are in italics. Clearly, the interface layer could be in various possible lateral positions with respect to the surrounding slabs. We considered all possible variations (top, fcc, hcp-hollow, bridge sites) yielding 16 different configurations for each interface type.

We also consider more complex interface geometries, based on the three bulk phases of  $Si_3N_4$ . In particular, one

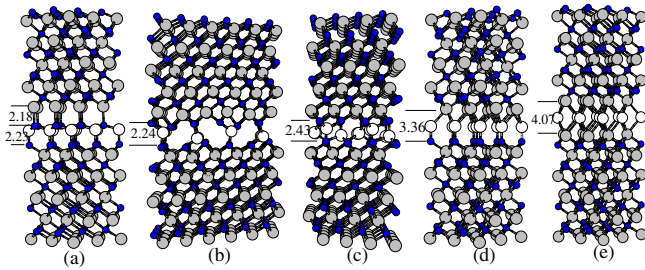


FIG. 1 (color online). Low energy interfaces: (a) ( $1 \times 1$ ) top-top-SiN, (b)  $\beta$ -like ( $1 \times 3$ )- $Si_2N_3$ , (c)  $\gamma$ -like ( $2 \times 2$ )- $Si_3N_4(4)$ , (d) ( $1 \times 1$ ) top-hcp-Si, and (e) ( $1 \times 1$ ) hcp-fcc-TiSi. Small dark, large gray, and white circles represent N, Ti, and Si atoms, respectively. Selected interlayer distances are given in Å.

complete layer of ( $10\bar{1}0$ ) $\alpha$ -, ( $10\bar{1}0$ ) $\beta$ -, and ( $111$ ) $\gamma$ - $Si_3N_4$ , with lateral unit cells of ( $2 \times 3$ ) (giving 148 atoms in the cell), ( $1 \times 3$ ) (74 atoms), and ( $2 \times 2$ ) (94 atoms), respectively. In addition, we also consider thinner “ $Si_3N_4$  derived” layers in which all Ti, N, and Si atoms are coordinated to their neighbors as in bulk TiN and  $Si_3N_4$ . Specifically, for the  $\beta$ -like interface (6.50 Å thick, not depicted), two layers of 2.24 and 4.26 Å are considered, which are denoted as “ $\beta$ -like  $Si_2N_3$ ” and “ $\beta$ -like  $Si_4N_5$ ,” respectively. Similarly, for the  $\gamma$ -like interface (4.52 Å thick, not depicted), two thinner interface structures are also considered, namely,  $\gamma$ -like  $Si_3N_4$  films of 2.09 and 2.43 Å, respectively. Since the Si atoms in the former structure are sixfold coordinated to the surrounding N atoms, we call it “ $\gamma$ -like  $Si_3N_4(6)$ ,” and in the latter they are fourfold coordinated, thus labeled “ $\gamma$ -like  $Si_3N_4(4)$ .” Further details of all these structures are given in Ref. [19].

The formation energies of all resulting 55 structures (except those which lie off the scale) are plotted in Fig. 2. It can be seen that, for nitrogen-rich conditions, the lowest energy structure is the  $\beta$ -like  $Si_2N_3$  [Fig. 1(b)] configuration and the next most favorable, the  $\gamma$ -like  $Si_3N_4(4)$  structure [Fig. 1(c)], followed by top-top-SiN [Fig. 1(d)]. In all of these structures, the Si atoms are bonded only to N atoms. These configurations are consistent with x-ray photoelectron spectroscopy results [5,6]; in particular, the calculated difference between the Si  $2p$  core level in bulk  $Si_3N_4$  and these interfaces is very similar to experiment, while the differences for the interfaces involving Ti-bonded Si are not. For lower (more negative) values of the chemical potential, the hcp-fcc-TiSi (Ti-Si-Ti bonded) interface is preferred. We note that the calculated vibrational and entropic contributions to the free energies of formation for the  $\beta$ -like  $Si_2N_3$  interface for tempera-

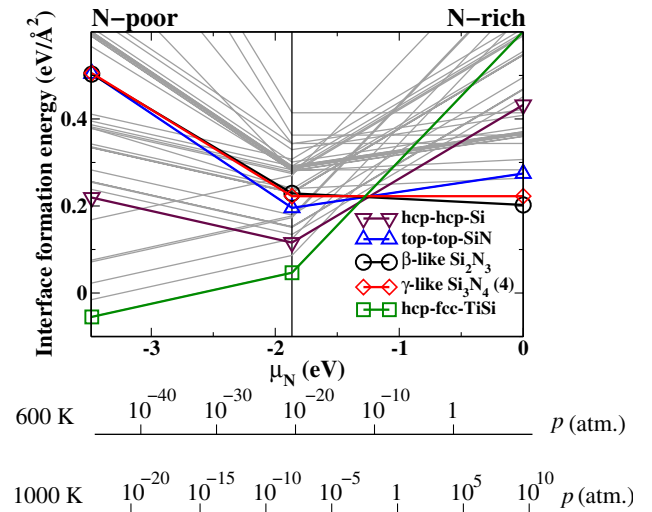


FIG. 2 (color online). Interface formation energies as a function of the nitrogen chemical potential  $\mu_N$ . The nitrogen chemical potential has been correlated with the pressure for two temperatures of 600 and 1000 K [cf. Eq. (2)] and is given with respect to half the total energy of  $N_2$ .

tures up to 1000 K are very small ( $\leq |3| \text{meV}/\text{\AA}^2$ ) and thus do not significantly affect the relative stabilities [24]. For the experimental conditions used in the works of Veprek *et al.* [5,13] ( $T = 773 \text{ K}$ ,  $p = 10^{-4} \text{ atm}$ ) and Meng *et al.* [14] ( $T = 523 \text{ K}$ ,  $p \approx 2.3 \times 10^{-7} \text{ atm}$ ), in which a hardness of 50–60 GPa and a hardness of  $< 35 \text{ GPa}$  was obtained, respectively, Fig. 2 indicates that, on *thermodynamic* grounds, the most stable interface geometry is the  $\beta$ -like  $\text{Si}_2\text{N}_3$ . The different hardnesses could be due to the lower temperature employed in the work of Ref. [14], which may kinetically hinder the system in reaching equilibrium. Alternatively, a cause may be oxygen contaminants, the effect of which we explore below.

In the search for new super- and ultrahard materials, often structures with high values of the bulk modulus and shear modulus are sought. A more stringent test may be provided by the ideal strength, i.e., the stress at which a crystal becomes mechanically unstable [25]. By determining the stresses along various inequivalent crystallographic directions, the weakest link that sets the limit on the material strength can be identified. In the following, we calculate the ideal strength of the interfaces, as well as various bulk systems. To do this, a tensile strain is applied perpendicular to the plane of the interface (or of the crystallographic plane of interest for the bulk systems), i.e., an elongation along the loading axis. We then determine the stress from the derivative of the total energy with respect to the strain, divided by the initial volume. The lateral dimensions of the supercells are kept constant during this process. We consider both (i) applying a uniform strain and (ii) allowing certain atomic relaxations (explained below). The results for (i) are shown in Fig. 3(a). It can be clearly seen that  $\text{TiN}\langle 111 \rangle$  has the highest tensile strength, where it is greater than 90 GPa. This value is very similar to the tensile strength of diamond in the  $\langle 111 \rangle$  direction, which is notably less than in the other directions, and limits the critical stresses that diamond can withstand [26]. The structures with the next highest strength are all the interfaces, followed by bulk  $\beta$ - $\text{Si}_3\text{N}_4$  in the  $\langle 10\bar{1}0 \rangle$  direction.  $\text{TiN}\langle 110 \rangle$  and  $\text{TiN}\langle 100 \rangle$  have the lowest strength.

In the second approach, we do as for (i) but fix the positions of the atoms in the upper and lower layers of the slab and relax all other atoms. In this case, bonds break

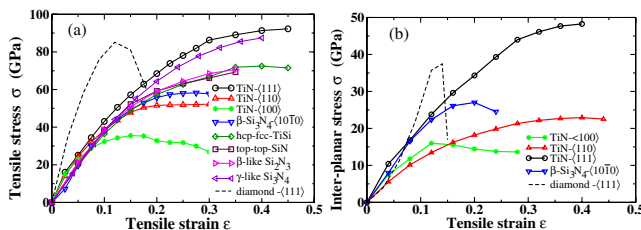


FIG. 3 (color online). Tensile stress for various low energy interface and bulk systems: (a) for a uniform strain and (b) for applying strain only between two atomic planes and thereby deliberately breaking the bonds.

at the interface and the strength is reduced compared to that of approach (i). This can be seen from Fig. 4 (solid curves).

For the bulk systems, to compare more closely with the strength of the relaxed interface systems, we deliberately break the bonds between a plane of atoms by applying strain only between the two atomic planes involved. Full atomic relaxation of all the other atoms is carried out. The results are shown in Fig. 3(b). The values of the strength are considerably smaller than those of Fig. 3(a) (and more similar to the values in Fig. 4), but the same trend is found as in Fig. 3(a). Comparing these values to those of the four interface systems (Fig. 4, solid curves), we can notice that the strength of bonding between  $\text{TiN}\langle 111 \rangle$  planes is still the highest ( $\sim 48 \text{ GPa}$ ) and that of the interface system  $\beta$ -like  $\text{Si}_2\text{N}_3$  has the next highest strength ( $\sim 35 \text{ GPa}$ ). After these two, bulk  $\beta$ - $\text{Si}_3\text{N}_4\langle 10\bar{1}0 \rangle$  interplanar bonding is next highest ( $\sim 27 \text{ GPa}$ ). Given that the strength of bonding between  $\text{TiN}\langle 111 \rangle$  planes is the greatest, it indicates that the enhanced hardness of the *nc*- $\text{TiN}/a$ - $\text{Si}_3\text{N}_4$  nanocomposites is primarily due to their affording and enhancing predominant interfaces involving the polar  $\text{TiN}\langle 111 \rangle$  planes. Figures 3(a) and 3(b) show that the strength of diamond in the  $\langle 111 \rangle$  direction is greater than that of the  $\beta$ -like  $\text{Si}_2\text{N}_3$  interface, consistent with measured hardness results.

We now address the effect of oxygen on the strength of the interface systems. We first determined the preferred adsorption site in the  $(1 \times 1)$  top-top-SiN and hcp-fcc-TiSi interfaces and the  $\beta$ -like  $\text{Si}_2\text{N}_3$  and  $\gamma$ -like  $\text{Si}_3\text{N}_4(4)$  interfaces. For the  $(1 \times 1)$  interfaces, we investigate both “high” and “low” oxygen concentrations, where for the latter, we use larger  $(2 \times 2)$  cells.

For the top-top-SiN interface, for nitrogen-rich conditions, for both low and high concentrations, oxygen prefers to occupy an interstitial site at the interface. For the  $(1 \times 3)$   $\beta$ -like  $\text{Si}_2\text{N}_3$  interface, a N-substitutional site at the interface is most favorable, as is the case for the  $\gamma$ -like  $\text{Si}_3\text{N}_4(4)$  interface. Thus, for these three interfaces, favored under nitrogen-rich conditions, oxygen will diffuse to the inter-

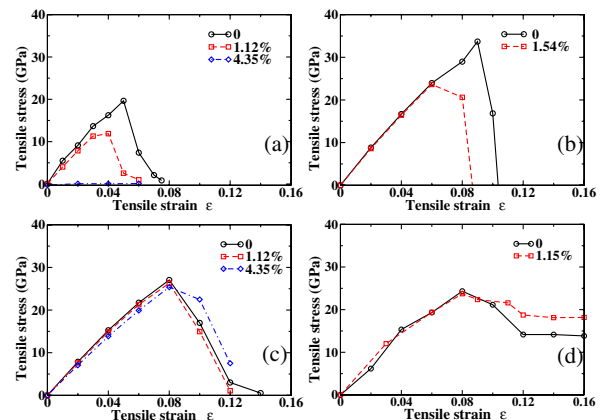


FIG. 4 (color online). Tensile stress with no oxygen (solid curve) and with different oxygen concentrations as indicated (see text) for the (a) top-top-SiN, (b)  $\beta$ -like  $\text{Si}_2\text{N}_3$ , (c) hcp-fcc-TiSi, and (d)  $\gamma$ -like  $\text{Si}_3\text{N}_4(4)$  interfaces.

face region. For the hcp-fcc-TiSi interface, oxygen prefers to occupy a N-substitutional site outside the Ti-Si-Ti interface.

The tensile strength of the interfaces with O impurities is presented in Fig. 4 (dashed and dotted-dashed lines), which include full atomic relaxation. For the top-top-SiN and  $\beta$ -like Si<sub>2</sub>N<sub>3</sub> interfaces, oxygen induces a significant reduction in the strength. For the former, oxygen binds strongly to the Ti atoms causing Ti-N bonds to break at the interface. For the  $\beta$ -like Si<sub>2</sub>N<sub>3</sub> interface, the presence of oxygen causes different bonds to break as compared to without oxygen: Here in the local vicinity of the oxygen impurity, the Si-O and the lower Ti-N bonds break, in contrast to the “upright,” single Si-N bonds for the case of no oxygen. We attribute this behavior to the greater bond strength of O to Ti as compared to Si [27], which has the effect of weakening (and elongating by 12%), and ultimately breaking under applied strain, the bond the Ti atoms have with the N atoms.

For the  $\gamma$ -like Si<sub>3</sub>N<sub>4</sub>(4) and hcp-fcc-TiSi interfaces, oxygen does not cause any reduction in the strength since the structure breaks at weaker bonds at the interface, not involving oxygen atoms. Thus, we find that the effect of oxygen on the strength of the interface depends on the details of the atomic geometry—for the theoretically predicted relevant interface, it induces a distinct weakening of the system. This mechanism may be responsible for the lower reported hardnesses.

In summary, from first-principles calculations, we predict the atomic geometry of interfaces occurring in the novel superhard and highly thermally stable *nc*-TiN/ $\alpha$ -Si<sub>3</sub>N<sub>4</sub> nanocomposite. The favorable interface formed under the technically relevant N-rich conditions involves a Si layer tetrahedrally coordinated to N atoms. The tensile strength of TiN in the  $\langle 111 \rangle$  direction is found to be notably greater than in the  $\langle 100 \rangle$  and  $\langle 110 \rangle$  directions and also greater than that of the interface systems. We predict that the enhanced hardness of these nanocomposites is related to their affording and enhancing predominant interface formation involving the polar TiN(111) planes with a thin polar partial  $\beta$ -Si<sub>3</sub>N<sub>4</sub> (10 $\bar{1}$ 0) layer. Oxygen impurities are predicted to diffuse to the interface region, giving rise to a striking reduction in the tensile strength. This deteriorating effect signals the importance of avoiding oxygen contamination for the practical creation of the nanocomposites if super- and ultrahard materials are desired.

We gratefully acknowledge the Australian Partnership for Advanced Computing National Facility and the Australian Center for Advanced Computing and Communications. This work was supported by the Australian Research Council. Financial support by the European Commission within the 6th Framework Programme under Contract No. AST 3-CT-2003-502741 “MACHERENA” is acknowledged.

- [1] S. Veprek, *J. Vac. Sci. Technol. A* **17**, 2401 (1999).
- [2] X. Blase *et al.*, *Phys. Rev. Lett.* **92**, 215505 (2004).
- [3] F. Gao *et al.*, *Phys. Rev. Lett.* **91**, 015502 (2003).
- [4] A. Y. Liu and M. L. Cohen, *Science* **245**, 841 (1989).
- [5] S. Veprek *et al.*, *Surf. Coat. Technol.* **133–134**, 152 (2000).
- [6] S. Veprek and S. Reiprich, *Thin Solid Films* **268**, 64 (1995).
- [7] V. V. Brazhkin, A. G. Lyapin, and R. J. Hemley, *Philos. Mag. A* **82**, 231 (2002).
- [8] W. D. Sproul, *Science* **273**, 889 (1996).
- [9] D. M. Teter, *MRS Bull.* **23**, 22 (1998).
- [10] M. Jilek *et al.*, *Plasma Chem. Plasma Process.* **24**, 493 (2004).
- [11] S. Veprek *et al.*, *Thin Solid Films* **476**, 1 (2005).
- [12] S. Veprek, S. Reiprich, and L. Shizhi, *Appl. Phys. Lett.* **66**, 2640 (1995).
- [13] S. Veprek *et al.*, *J. Vac. Sci. Technol. B* **22**, L5 (2004).
- [14] W. J. Meng *et al.*, *J. Mater. Res.* **17**, 2628 (2002).
- [15] H. Söderberg *et al.*, *J. Appl. Phys.* **97**, 114327 (2005).
- [16] X. Hu *et al.*, *J. Vac. Sci. Technol. A* **23**, 114 (2005).
- [17] B. Delley, *J. Chem. Phys.* **92**, 508 (1990); **113**, 7756 (2000).
- [18] J. P. Perdew, K. Burke, and M. Ernzerhof, *Phys. Rev. Lett.* **77**, 3865 (1996).
- [19] S. Hao, B. Delley, and C. Stampfl, *Phys. Rev. B* **74**, 035402 (2006); **74**, 035424 (2006).
- [20] C. Iwamoto and S. Tanaka, *J. Am. Ceram. Soc.* **81**, 363 (1998).
- [21] For the Si atom chemical potential  $\mu_{\text{Si}}$  under nitrogen-rich conditions, we assume an upper limit determined by bulk  $\beta$ -Si<sub>3</sub>N<sub>4</sub>, that is,  $\mu_{\text{Si}_3\text{N}_4} = 3\mu_{\text{Si}} + 4\mu_{\text{N}}$ , where  $\mu_{\text{Si}_3\text{N}_4}$  is the chemical potential of bulk  $\beta$ -Si<sub>3</sub>N<sub>4</sub>. Then we have  $\mu_{\text{Si}} = \frac{1}{3}(E_{\text{tot}}^{\text{Si}_3\text{N}_4} - 2E_{\text{tot}}^{\text{N}_2})$ , where  $E_{\text{tot}}^{\text{Si}_3\text{N}_4}$  is the total energy of a bulk unit of  $\beta$ -Si<sub>3</sub>N<sub>4</sub>. For N-poor conditions, we assume an upper limit of the Si chemical potential determined by bulk TiSi<sub>2</sub>, that is,  $\mu_{\text{TiSi}_2} = \mu_{\text{Ti}} + 2\mu_{\text{Si}}$ , where  $\mu_{\text{TiSi}_2}$  is the chemical potential of bulk TiSi<sub>2</sub>. Then we have  $\mu_{\text{Si}} = \frac{1}{2}(E_{\text{tot}}^{\text{TiSi}_2} - E_{\text{Ti}}^{\text{bulk}})$ , where  $E_{\text{tot}}^{\text{TiSi}_2}$  is the total energy of a bulk unit of TiSi<sub>2</sub>. This is explained in more detail in Ref. [19].
- [22] K. Reuter and M. Scheffler, *Phys. Rev. B* **65**, 035406 (2002).
- [23] JANAF tables: M. W. Chase, C. A. Davies, J. R. Downey, D. J. Frurip, R. A. McDonald, and A. N. Syverud, *J. Phys. Chem. Ref. Data* **14**, 1551 (1985), Suppl. No. 1.
- [24] We calculate the contribution to the free energy from the vibrational frequencies  $\omega_i$  by constructing and diagonalizing the dynamical matrix and then using the equation  $E_{\text{vib}}(T, \omega) = 1/(2\pi)^3 [\sum_i \frac{1}{2} \hbar \omega_i + k_B T \ln\{1 - \exp[-(\hbar \omega_i/k_B T)]\}]$ , where  $k_B$  is the Boltzmann constant.
- [25] J. W. Morris, Jr. *et al.*, *Phase Transformations and Evolution in Materials*, edited by P. E. Turchi and A. Gonis (The Minerals, Metals and Materials Society, Warrendale, PA, 2000).
- [26] R. H. Telling *et al.*, *Phys. Rev. Lett.* **84**, 5160 (2000).
- [27] *Handbook of Chemistry and Physics*, edited by R. C. Weast, M. J. Astle, and W. H. Beger (Chemical Rubber Company, Boca Raton, 1988), Vol. 69.